RSC Advances

PAPER

View Article Online
View Journal | View Issue

Check for updates

Cite this: *RSC Adv.*, 2020, **10**, 17154

MOF-derived (MoS_2, γ-Fe_2O_3)/graphene Z-scheme photocatalysts with excellent activity for oxygen evolution under visible light irradiation†

Ang Li,[a] Yuxiang Liu,[a] Xuejun Xu,[b] Yuanyuan Zhang,[a] Zhichun Si, *[a] Xiaodong Wu,[c] Rui Ran[c] and Duan Weng[ac]

Received 5th March 2020
Accepted 17th April 2020

DOI: 10.1039/d0ra02083d

rsc.li/rsc-advances

Constructing Z-scheme heterojunctions is considered as an effective strategy to obtain catalysts of high efficiency in electron–hole separation in photocatalysis. Unfortunately, suitable heterojunctions are difficult to fabricate because the direct interaction between two semiconductors may lead to unpredictable negative effects such as electron scattering or electron trapping due to the existence of defects which causes the formation of new substances. Furthermore, the van der Waals contact between two semiconductors also results in bad electron diffusion. In this work, a MOF-derived carbon material as a Z-scheme photocatalyst was synthesized *via* one-step thermal treatment of MoS_2 dots @Fe-MOF (MIL-101). Under visible light irradiation, the well-constructed Z-scheme (MoS_2, γ-Fe_2O_3)/graphene photocatalyst shows 2-fold photocatalytic oxygen evolution activity (4400 μmol g^{-1} h^{-1}) compared to that of γ-Fe_2O_3/graphene (2053 μmol g^{-1} h^{-1}). Based on ultraviolet photoelectron spectrometry (UPS), Mott–Schottky plot, photocurrent and photoluminescence spectroscopy (PL) results, the photo-induced electrons from the conduction band of γ-Fe_2O_3 could transport quickly to the valence band of MoS_2 *via* highly conductive graphene as an electron transport channel, which could significantly enhance the electron–hole separation efficiency as well as photocatalytic performance.

Open Access Article. Published on 01 May 2020. Downloaded on 2/13/2026 8:04:32 PM.
This article is licensed under a Creative Commons Attribution-NonCommercial 3.0 Unported Licence.

1. Introduction

With the huge consumption of fossil energy resulting in serious environmental and social problems, the production and application of clean energies have become hot topics in the 21st century. Utilizing sunlight and water to generate a clean energy, hydrogen, *via* photocatalytic or photoelectrocatalytic water splitting is considered as an ideal strategy to solve these energy and environmental problems in the future.[1–3] The water splitting reaction consists of water reduction (hydrogen evolution reaction, HER) and water oxidation (oxygen evolution reaction, OER).[4] Since the oxygen evolution reaction is a four-hole reaction and the reaction rate is rather slow, it is always considered to be the rate-determining step of the overall photocatalytic water splitting reaction.[5,6]

Among the catalysts for photocatalytic oxygen evolution, iron oxide is one of the most promising materials with advantages of earth abundant, nontoxic to the environment, and responsive to almost the whole visible region of the solar spectrum.[7] However, the intrinsic deficiencies of Fe_2O_3, such as short diffusion lengths of photo-induced holes and low electroconductivity, restrain its practical applications.[8–10] Doping by metal/non-metal elements (such as Al/Fe_2O_3,[11,12] Ti/Fe_2O_3,[13] S,N/Fe_2O_3 (ref. 14)), constructing composite catalysts (ZnO/Fe_2O_3,[15] WO_3/Fe_2O_3 (ref. 16)) and synthesizing iron oxide nanoparticles of specific morphology[17–19] have been adopted to improve the catalytic performance of Fe_2O_3. Among these approaches, constructing Z-scheme heterojunctions is considered to be an efficient method due to enhanced charge separation efficiency of Fe_2O_3. Cong *et al.* prepared Fe_2O_3–MoS_2–Cu_2O nanocomposites by electrodeposition and hydrothermal methods. Thanks to the distinctive electron–hole pair separation *via* Z mechanism, the photoelectrochemical performance was improved. However, limited by poor electronic conduction between semiconductors, the photocatalytic performances of these Z scheme photocatalysts are not good enough and other strategies need to be developed for further improvement of photocatalytic performance.[20]

Various carbon-based materials have been designed and applied to photocatalysis and energy storage fields. The main advantages of carbon-based materials include high electrical conductivity, large specific surface area, good mechanical strength and portability. Embedding semiconductor

[a]*Tsinghua Shenzhen International Graduate School, Tsinghua University, Shenzhen City, 518055, China. E-mail: si.zhichun@sz.tsinghua.edu.cn*

[b]*College of Materials Science and Energy Engineering, Foshan University, Foshan City, 528000, China*

[c]*The Key Laboratory of Advanced Materials of Ministry of Education, School of Materials Science and Engineering, Tsinghua University, Beijing City, 10084, China*

† Electronic supplementary information (ESI) available. See DOI: 10.1039/d0ra02083d

This journal is © The Royal Society of Chemistry 2020

Open Access Article. Published on 01 May 2020. Downloaded on 2/13/2026 8:04:32 PM.
This article is licensed under a Creative Commons Attribution-NonCommercial 3.0 Unported Licence.

photocatalyst into carbon materials, such as graphene or reduced graphene oxide (RGO), exhibited outstanding photocatalytic performance.[21–23] Han *et al.* reported that the composite of Fe_2O_3 and graphene achieved significantly enhanced photocatalytic performance, and proved that the high conductivity of graphene helps the transfer and storage of photogenerated electrons from Fe_2O_3.[24] Chen *et al.* fabricated a 3D quasi-hierarchical Z-scheme RGO-Fe_2O_3–MoS_2 nanocomposite and obtained enhanced MB photocatalytic degradation performance.[25] During the photocatalytic reaction, the RGO layers act as the current collector to enhance carriers transport, and form the heterojunctions with Fe_2O_3 and MoS_2 to promote the separation of photogenerated carriers.

Recently, the carbon materials derived from metal–organic frameworks (MOFs) have been widely studied in battery materials and catalysis.[26–29] Thanks to the high BET surface areas, the tunability of the metal–organic combination and diverse structures, MOFs have become promising sacrificial templates and precursors for the preparation of carbon-based nanomaterials.[30] Compared with other carbon materials, MOF-derived carbon nanomaterials have great advantages in terms of large porosity and easy functionalization with metal/metal oxides, which make them highly efficient for numerous reactions. In this work, well-constructed MoS_2/graphene/γ-Fe_2O_3 ternary heterojunctions were fabricated *via* one-step calcination of the MoS_2 dots @Fe-MOF composite under inert atmosphere at elevated temperature. To our knowledge, this is the first report of a MOF-derived carbon material as the Z-scheme photocatalyst. Photocatalytic oxygen evolution for the MoS_2/graphene/γ-Fe_2O_3 heterojunctions were tested and the mechanism for photocatalytic water oxidation reaction was proposed. According to this scheme, more Z-scheme photocatalysts could be constructed, and it would be helpful for the application of MOF-derived carbon materials in photocatalysis.

2. Experimental

2.1 Materials

All the chemicals used were AR purity without further purification. Thiourea (CH_4N_2S, 99%), hexaammonium molybdate tetrahydrate ($(NH_4)_6Mo_7O_{24}\cdot 4H_2O$, 99%), iron chloride hexahydrate ($FeCl_3\cdot 6H_2O$, 99%), dimethylformamide (DMF, 99.5%), *p*-phthalic acid (PTA, 99%) and silver nitrate ($AgNO_3$, 99.8%) were purchased from Aladdin Corp. Nafion D520 dispersion was purchased from Alfa Aesar.

2.2 Synthesis of MoS_2 dots

Bulk MoS_2 sheets were synthesized according to the previous work.[31] Firstly, 2 mmol $(NH_4)_6Mo_7O_{24}\cdot 4H_2O$ and 60 mmol CH_4N_2S were dissolved in 70 mL water. After continuous stirring for 30 min, the homogeneous solution was transferred into a 100 mL Teflon-lined stainless steel autoclave and heated for 18 h at 230 °C. After cooling down to the room temperature, the black precipitate was washed by water and ethanol for several times, and dried in vacuum for 12 h at 60 °C.

MoS_2 dots were obtained through an ultrasonic exfoliation method. 10 mg bulk MoS_2 powder was dispersed in 200 mL ethanol in a beaker, and then ultrasonically grinded for 3 h (FS-450N, ShengXi Ultrasonic Instrument Co. Shanghai, China). Then the suspension was transferred to a 250 mL volumetric flask and calibrated to 250 mL with ethanol. Finally, the MoS_2 dots ethanol solution with a concentration of 40 mg L^{-1} was obtained.

2.3 Synthesis of MIL-101(Fe)

MIL-101(Fe) was synthesized using the previously-reported method.[32] Terephthalic acid (0.824 g, 4.96 mmol) and iron chloride hexahydrate ($FeCl_3\cdot 6H_2O$, 2.649 g, 9.8 mmol) were dissolved in dimethylformamide (DMF, 60 mL). The mixture was transferred to a 100 mL Teflon-lined stainless steel autoclave and heated at 110 °C for 20 h. After cooling to room temperature naturally, the generated precipitate was collected by centrifugation at 8000 rpm for 10 min, washed with ethanol more than 3 times and dried in vacuum at 60 °C for 12 h.

2.4 Synthesis of MM (MoS_2/MIL-101(Fe))

MoS_2/MIL-101(Fe) was synthesized *via* an impregnation method. To be specific, 0.5 g MIL-101(Fe) was dissolved in the solution of MoS_2 dots (concentration of MoS_2 is 40 mg L^{-1}). After stirring for 24 h, the solution was dried at 85 °C in air to remove ethanol and then dried in vacuum at 60 °C for 12 h to obtain MoS_2/MIL-101(Fe) catalyst (MM).

2.5 Synthesis of FG (γ-Fe_2O_3/graphene) and MFG ((MoS_2, γ-Fe_2O_3)/graphene)

The precursor, MIL-101(Fe) and MoS_2/MIL-101(Fe), were heated to 500 °C with the heating rate of 5 °C min^{-1} in Ar. After calcination treatment for 4 hours, the carbonized samples were collected and labeled as FG and MFG catalysts.

2.6 Characterizations

Crystalline and phase structures of catalysts were characterized by a Bruker D8 Advance X-ray diffractometer (XRD) using Cu Kα ($\lambda = 1.5406$ Å) radiation. The microstructure and morphology were observed using field emission scanning electron microscopy (FESEM, HITACHI SU8010) and transmission electron microscopy (TEM, FEI TECNAI G2 F30). The molybdenum sulfide dots were characterized by atomic force microscope (AFM, MDTC-EQ-M16-01). Raman spectra were measured by a Raman microscope (HORIBA LabRAM HR800) at 532 nm excitation wavelength. The X-ray photoelectron spectra (XPS) data was recorded on PHI-5000 Versaprobe II instrument using a monochromatic Al Kα source to analyze the composition and chemical state. The accurate atom ratios were measured by coupled plasma emission spectrometry (ICP-OES, PE7300dv). The photoluminescence (PL) spectra were collected on a fluorescence spectrophotometer (Edinburgh Instruments FLS 980) with the excitation wavelength of 325 nm. The ultraviolet photoelectron spectrometer (UPS) tests were carried on the X-ray photoelectron spectra (Thermo Fisher, ESCALAB 250i) and

Open Access Article. Published on 01 May 2020. Downloaded on 2/13/2026 8:04:32 PM.
This article is licensed under a Creative Commons Attribution-NonCommercial 3.0 Unported Licence.

the Mott–Schottky (MS) tests were carried on the electrochemical workstation (Chenhua Shanghai, CHI660E).

2.7 Photocatalytic activity measurements

The photocatalytic oxygen evolution reaction activities of catalysts were carried out on a testing apparatus from Ceaulight Company (CEL-SPH2N-D9). The produced oxygen was measured by a gas chromatography (Ceaulight, GC-7920) and high purity argon was used as carrier gas. Briefly, 10 mg of photocatalyst powder was dispersed into 100 mL ultra-pure water containing sacrificial reagent (0.01 M $AgNO_3$) and vacuumized more than 30 minutes to remove oxygen in the solution. A 300 W Xe lamp (Ceaulight, CEL-HXF300) with a 400 nm cut-off filter was applied as visible light source and the incident light intensity was 100 mW cm^{-2} on average.

2.8 Photoelectrochemical measurements

Photocatalyst for photoelectrochemical characterization is pretreated and the experiments were carried out in a three-electrode system. Briefly, 10 mg photocatalyst was dispersed in 400 μL isopropanol containing 20 μL of Nafion solution under ultrasonication for half an hour. Then, pipetted 20 μL of the mixed solution with a pipette and spin-coated it on the conductive side of ITO glass with size of 1 cm × 1 cm. Finally, samples were dried in vacuum at 60 °C for 6 hours and working electrode was prepared. Platinum plate was used as the counter electrode and Ag/AgCl (3.5 M KCl) electrode as reference electrode. 100 mL of 0.1 M Na_2SO_4 aqueous solution was used for electrolyte. The transient photocurrent measurements were carried out with a bias voltage of 0.2 V *vs.* Ag/AgCl and 20 s on/off period. The MS plots were measured under frequency of 1000 Hz in the dark environment.

3. Results and discussion

3.1 Structural and morphological analyses

Evenly dispersed MoS_2 was prepared by ultrasonically crushing bulk MoS_2 sheets into nanodots. The atomic force microscope (AFM) is used to characterize the size of MoS_2 dots. The thickness of the molybdenum sulfide dots obtained by the ultrasonic vibration grinding treatment was 5–20 nm (Fig. 1).

SEM images of MIL-101(Fe), MM, FG and MFG were recorded to explore the microstructure and morphology of the materials. The morphology of MIL-101(Fe) is an octahedral structure in size of 0.5–3 μm (Fig. 2(a)). The MM maintains the octahedron morphology of MIL-101(Fe) with rough surface as result of the loading of MoS_2 dots (Fig. 2(b)). As shown in Fig. 2(c), MIL-101(Fe) transformed to octahedral γ-Fe_2O_3 in size of 100–500 nm and graphene substrate after calcination, which is consistent with previous results.[33] At the initial stage of calcination, the iron oxide clusters crystallized on the octahedral surface during the gradual decomposition of MIL-101(Fe). The contraction force derived from the iron oxide crystallite leads to the inward contraction of the surface Fe_2O_3 layer. Due to the smaller size, carbon atoms diffuse out in form of the interstitial solute atoms and form graphene under the catalysis of iron. Eventually, a structure in which octahedral iron oxide supported on graphene is formed. When rising the temperature of MM heating treatment, highly dispersed γ-Fe_2O_3 octahedrons around 100–500 nm and MoS_2 dots (5–10 nm) located on graphene substrate could be obtained (Fig. 2(d)).

The phase purity and crystal structure of the MFG were examined by X-ray diffraction (XRD). The XRD patterns in Fig. 3(a) and S1† show that the main phase of iron oxide in MFG and FG is γ-Fe_2O_3. The peaks at 30.2°, 35.6°, 37.2°, 43.3°, 53.7°,57.3°, 62.9°, 71.4° and 74.5° are obvious which are indexed to (220), (311), (222), (400), (511), (422), (440), (620) and (533) lattice planes of γ-Fe_2O_3 (JCPDS card 39–1346), respectively.[34] Peak at 26.5° is owing to (002) lattice planes of graphene. Another one at 39.6° is related to the (103) lattice planes of MoS_2, which could not be found in XRD pattern of FG (Fig. S1†), revealing the existence of MoS_2 in MFG.[35,36] The formation of graphene is further determined by Raman, which is shown in Fig. 3(b). Three peaks can be obtained from the figure, D peak (1329 cm^{-1}), G peak (1585 cm^{-1}) and 2D peak (2837 cm^{-1}), respectively. The integral intensity ratio of D band to G band (I_D/I_G) is 0.676, confirming that the MFG has a considerable degree of graphitization. The content of Mo was 1.4% and Fe was 44%

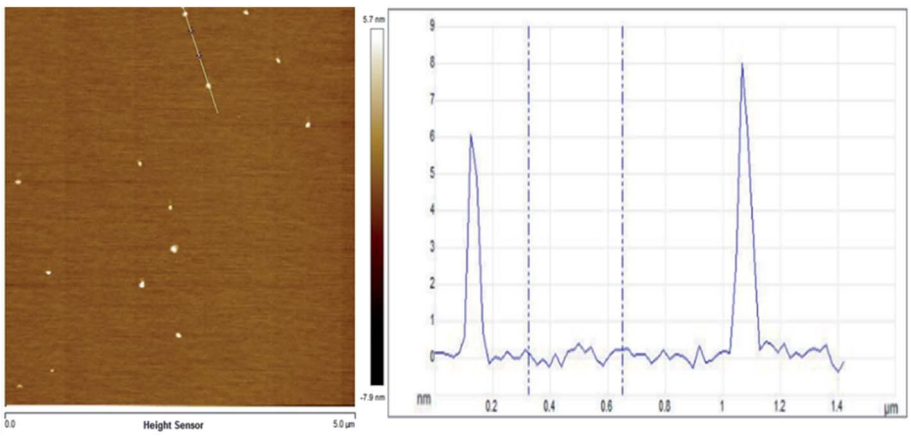

Fig. 1 AFM results of MoS_2 dots.

 This journal is © The Royal Society of Chemistry 2020

Open Access Article. Published on 01 May 2020. Downloaded on 2/13/2026 8:04:32 PM.
This article is licensed under a Creative Commons Attribution-NonCommercial 3.0 Unported Licence.

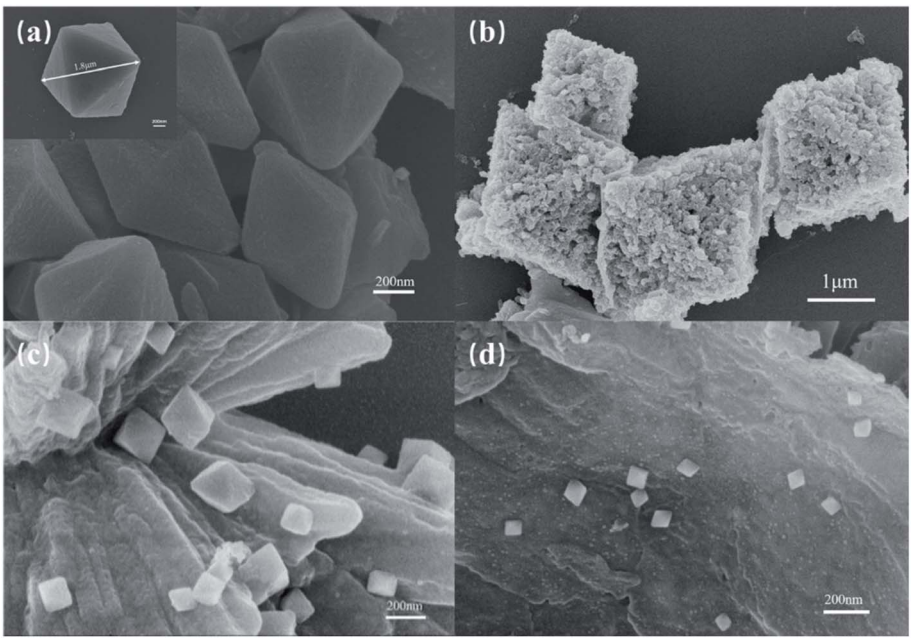

Fig. 2 SEM images of (a) MIL-101(Fe), (b) MoS_2/MIL-101(Fe), (c) γ-Fe_2O_3/graphene and (d) (MoS_2, γ-Fe_2O_3)/graphene.

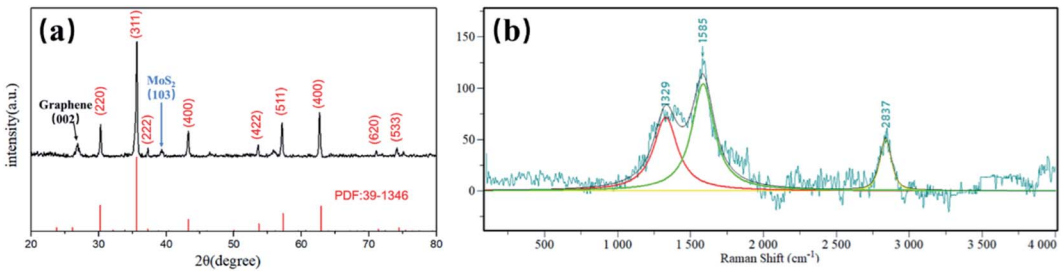

Fig. 3 (a) XRD pattern and (b) Raman spectra of MFG.

by ICP-OES shown in Table S1.† The peaks of MoS_2 cannot be distinguished in Raman spectrum due to its low content.

The microstructure of the MFG was characterized by TEM, and the results are shown in Fig. 4. The dark octahedral structures shown in Fig. 4(a) and (b) are γ-Fe_2O_3 particles and the particle size is 50–500 nm. The distinct distance of plane about 0.34 nm attributed to the interplanar spacing of (002) plane of graphene is observed in Fig. 4(b), revealing that the graphene of 3–5 layers formed *via* the decomposition of MOF-101. It can be seen from Fig. 4(c) that the large dark region has an interplanar crystal spacing of 0.25 nm, which corresponds to the (311) plane of γ-Fe_2O_3. Fig. 4(d) shows that the interplanar crystal spacing of 0.23 nm corresponds to the (103) plane of MoS_2.[36] The above results confirm that MoS_2/graphene/Fe_2O_3 heterojunctions are well constructed *via* the *in situ* thermal treatment of MoS_2/Fe-MOF composites, which is shown in Scheme 1.

XPS was used to investigate the surface chemical states of samples and the results are shown in Fig. 5. As shown in Fig. 5(a), the C 1s spectrum can be deconvoluted into several peaks, including the sp2 C–C bond of the graphene skeleton (C=C, 284.2 eV), sp^3 hybrid carbon (C–C/C–H, 285.2 eV), alcohol, epoxy and ether groups (C–O, 286.3 eV), carbonyl (C=O, 287.5 eV) and carboxylic acid/ester groups (–O–C=O, 289.3 eV), respectively.[37–39] As shown in Fig. 5(b), the O 1s spectrum can be deconvoluted into three peaks at 530.1, 531.8 and 533.3 eV, which are attributed to Fe–O, C=O and O–C=O, respectively. As shown in Fig. 5(c), the XPS peaks of Fe $2p_{1/2}$ (724.6 eV) and Fe $2p_{3/2}$ (711.3 eV) are assigned to the Fe_2O_3 and the peaks of Fe $2p_{1/2}$ (724.0 eV), satellite Fe $2p_{3/2}$ (713.4 eV) and Fe $2p_{3/2}$ (710.9 eV) are assigned to the Fe_3C phase in MFG.[40] As shown in Fig. 5(d), Mo shows two valence states in MM (MoS_2/MOF). In details, the XPS peaks of Mo $3d_{3/2}$ (228.7 eV) and Mo $3d_{5/2}$ (232.3 eV) correspond to Mo^{4+} in MoS_2, Mo $3d_{3/2}$ (232.8 eV) and Mo $3d_{5/2}$ (235.8 eV) correspond to Mo^{6+} in MoO_3.[41] The appearance of Mo^{6+} is mainly attributed to the surface oxidation of MoS_2 during ultrasonication. The MFG obtained by carbonization of MM has two more XPS peaks at 228.2 and 231.1 eV, which are attributed to the Mo–C bond formed during the carbonization of MM.[42] The XPS results shows the co-existence of Fe–C and Mo–C, which indicates the strong interaction between MoS_2/graphene and Fe_2O_3/graphene interfaces in MFG.

Open Access Article. Published on 01 May 2020. Downloaded on 2/13/2026 8:04:32 PM.
This article is licensed under a Creative Commons Attribution-NonCommercial 3.0 Unported Licence.

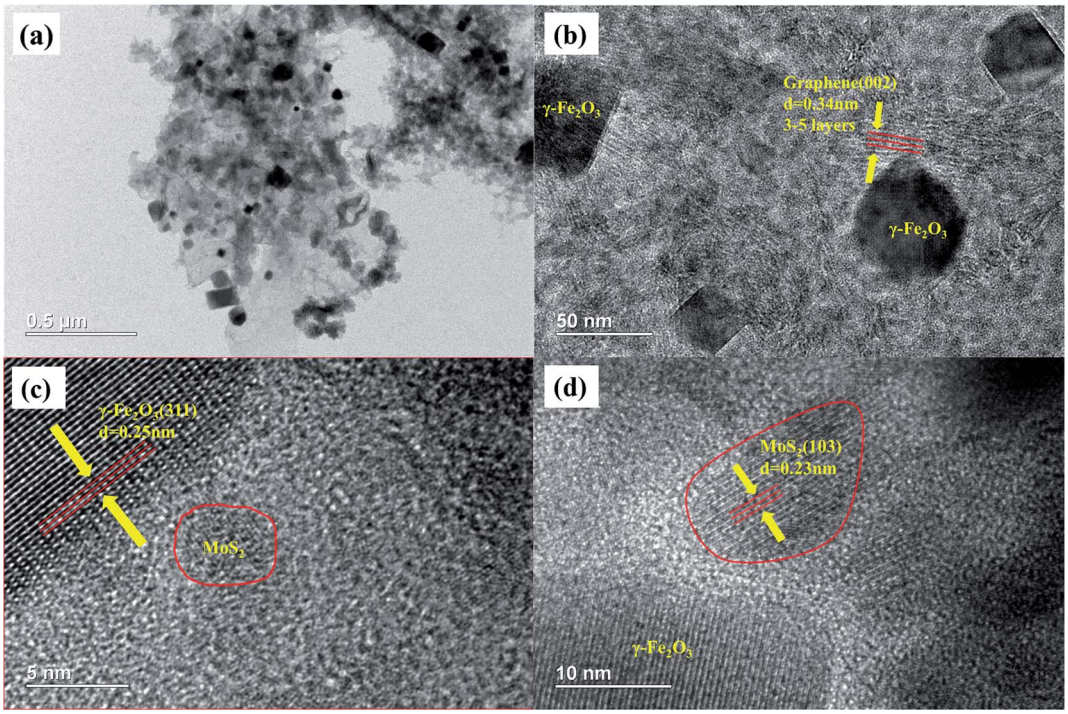

Fig. 4 (a) and (b) TEM images of MFG, (c) and (d) HRTEM images of MFG.

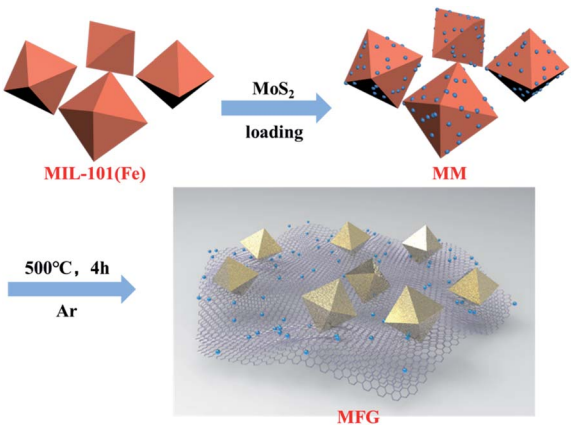

Scheme 1 The synthesis process of MFG.

3.2 Photocatalytic performance and discussion

The photocatalytic performance of the as-prepared α-Fe_2O_3, MIL-101, MM, FG and MFG was evaluated by oxygen evolution in 0.01 M $AgNO_3$ aqueous solution under visible light irradiation (Fig. 6(a) and (b)). A rate of 2053 μmol g^{-1} h^{-1} was detected with the catalyst MM for the first hour and an average oxygen evolution of 1637 μmol g^{-1} h^{-1} was recorded after three hours of irradiation. The FG obtained by carbonization of Fe-MOF showed comparable photocatalytic oxygen evolution activity to that of MM and pristine MIL-101. With the catalyst α-Fe_2O_3, which was obtained by heat treating MIL-101 in air at 500 °C for 4 hours, a rate of 180 μmol g^{-1} h^{-1} was detected in the first hour, and an average oxygen evolution of 130 μmol g^{-1} h^{-1} was recorded after three hours of irradiation. For MFG, the photocatalytic oxygen evolution activity of 4400 μmol g^{-1} h^{-1} was detected in the first hour, which was more than twice compared to that of MM and FG. After three hours of irradiation, the average photocatalytic oxygen evolution of 2262 μmol g^{-1} h^{-1} was recorded, which was 1.4 times as that of MM and FG.

To further explore the mechanism for the enhancement in the photocatalytic activity of MFG, energy band structure alignment and the charge-transfer and separation efficiency studies were carried out. Fig. 7(a) shows the photocurrents of the FG and MFG electrodes under visible light irradiation with the on/off period of the light irradiation 20 s. The photocurrent density of MFG is about 1.6 times as that of FG. The higher photocurrent density of MFG suggests that the photogenerated electron–hole pairs in MFG have higher separation efficiency and longer lifetime, which is beneficial to improve the photocatalytic activity. As shown in Fig. 7(b), the PL emission spectra is also consistent with the result of photocurrent density. The intensity of emission peak of MFG is much lower than that of FG, indicating that the photogenerated electron–hole pairs recombination is suppressed and the charge separation is improved.[43]

The UV-visible diffuse reflectance spectrums of the catalysts were shown in ESI (Fig. S2†). Since most of the composition of MFG and FG is carbon, which enhanced the absorption of light, the band gap cannot be studied by UV-visible diffuse reflectance spectrum. So, we chose the method of Mott–Schottky tests and UPS to study the energy band of the catalysts.

The valence band edge (E_{VB}) of the semiconductor can be estimated by UPS.[44–46] The preparation process of samples for tests is listed in ESI.† As shown in Fig. 8(a), the high binding

 This journal is © The Royal Society of Chemistry 2020

Open Access Article. Published on 01 May 2020. Downloaded on 2/13/2026 8:04:32 PM.
This article is licensed under a Creative Commons Attribution-NonCommercial 3.0 Unported Licence.

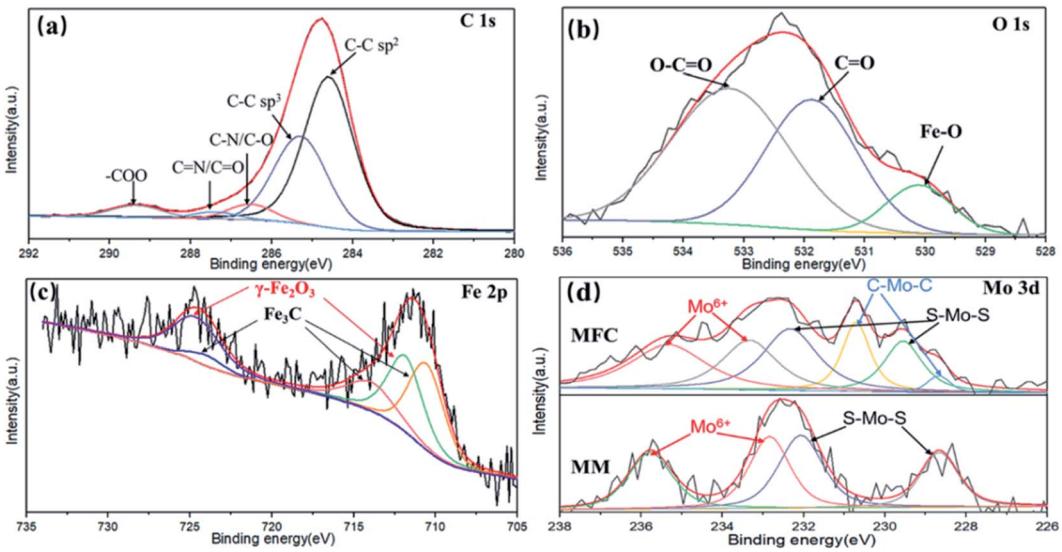

Fig. 5 XPS spectra of MFG: (a) C 1s, (b) O 1s, (c) Fe 2p and (d) Mo 3d.

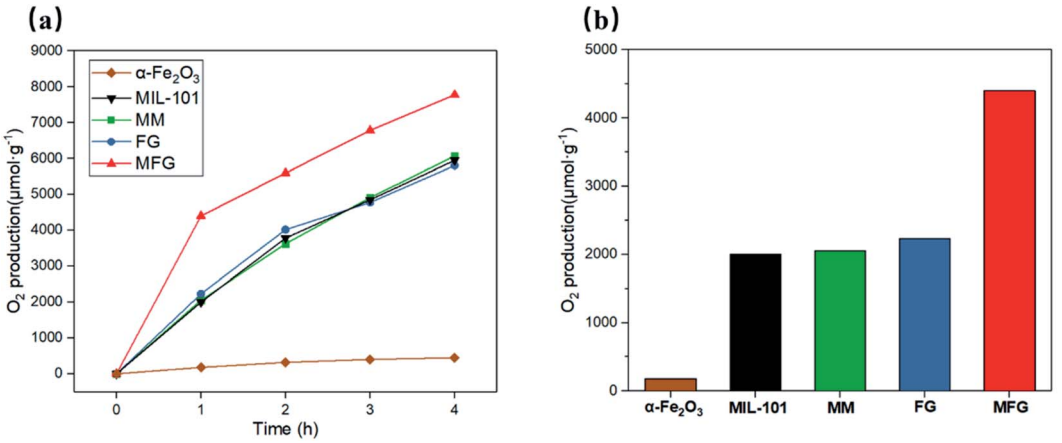

Fig. 6 (a) Photocatalytic oxygen evolution plots of α-Fe_2O_3, MIL-101, MM, FG and MFG under visible light; (b) photocatalytic oxygen evolution of α-Fe_2O_3, MIL-101, MM, FG and MFG under visible light in the first hour.

energy (BE) cutoff region (secondary electron cutoff edge, SEE) of MFG is 16.52 (±0.03) eV, which is consistent with FG. Fig. 8(b) shows the corresponding low binding energy portion of the UPS spectrum close to the Fermi level, with a tangent to get E_{onset} = 2.92 (±0.03) eV. The ionization potential of the FG and MFG samples under vacuum conditions is 7.62 (±0.06) eV calculated from the formula $\varphi = h\nu - (E_{cutoff} - E_{onset})$ with the excitation energy of the He I UPS spectrum 21.22 eV. The value of E_{VB} can be converted to an electrochemical potential according to a reference standard, where 0 V *vs.* RHE (reversible hydrogen electrode) is equal to 4.44 eV *vs.* evac (vacuum level), thereby the obtained E_{VB}s of the FG and MFG are 3.18 (±0.06) V *vs.* RHE. The potential of the conduction band edge (E_{CB}) of the semiconductor was estimated by the Mott–Schottky (MS) tests.[47] The MS plots of FG and MFG were measured at a frequency of 1000 Hz in the dark. As shown in Fig. 8(c), the positive slope of the linear MS curve reveals that FG and MFG are n-type semiconductors. The E_{CB} can be determined by the intercept on the *x*-axis in the MS plots. Compared with the Ag/AgCl electrode, the derived E_{CB} potential of FG in the aqueous solution is 0.15 V, while the MS curve of the MFG shifts to the negative direction of the coordinate axis. The derived E_{CB} potential of MFG in the aqueous solution is −0.03 V, which confirms that the bottom of the conduction band is extended to a more negative potential compared with that of FG.

Fig. 8(d) is a schematic diagram showing the band alignment of MFG and the possible mechanism of photocatalytic oxygen evolution on MFG catalysts.[43,48–50] Based on the above results, the E_{CB} potential of Fe_2O_3 is 0.15 eV and E_{VB} potential of Fe_2O_3 is 3.18 eV, while the E_{CB} potential of MoS_2 is −0.03 eV and the band gap of MoS_2 is 1.9 eV,[43] respectively. The band alignment of MFG is matched with Z-scheme. When light is irradiated onto the MFG, the photo-induced electron–hole pairs are generated in octahedral iron oxide and molybdenum sulfide. Due to the strong bonding with graphene substrate *via* Mo–C and Fe–C bond, the electrons in well crystalized iron oxide conduction

Open Access Article. Published on 01 May 2020. Downloaded on 2/13/2026 8:04:32 PM.
This article is licensed under a Creative Commons Attribution-NonCommercial 3.0 Unported Licence.

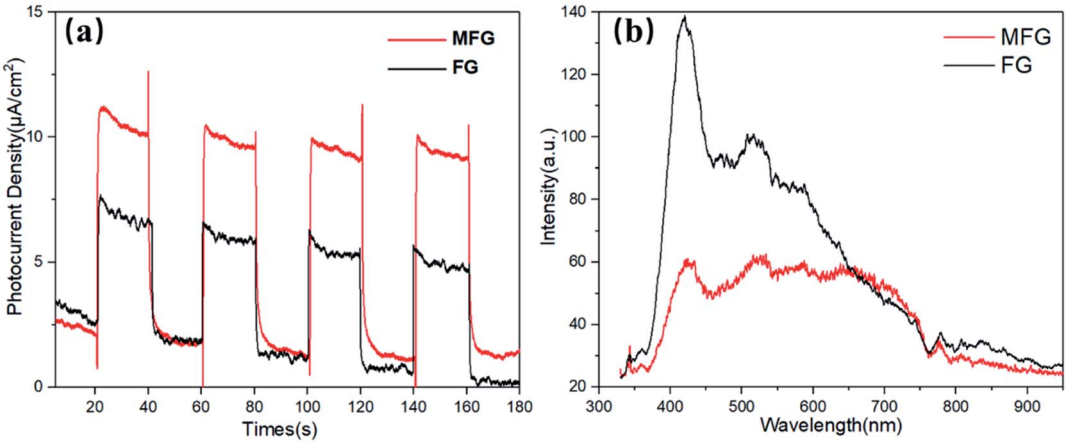

Fig. 7 (a) The periodic on/off photocurrent *vs.* irradiation time, (b) PL spectra of FG and MFG.

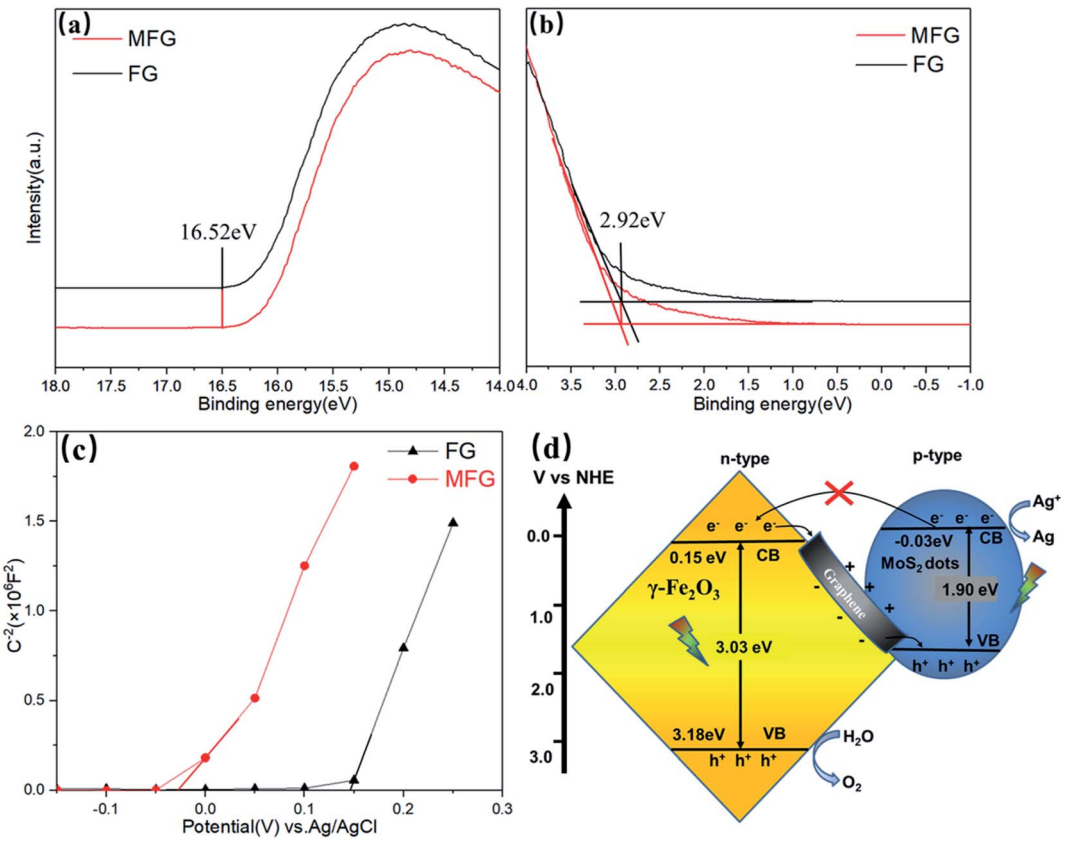

Fig. 8 (a) High binding energy cutoff region and (b) low binding energy portion of UPS spectra of MFG. (c) Mott–Schottky plots of FG and MFG. (d) A schematic illustration of the band structures of the MFG.

band can quickly transfer to the valence band of molybdenum sulfide through highly conductive graphene, and combine with the generated photogenerated holes. Thus, lifetime of photogenerated holes in iron oxide is significantly increased. At the same time, the electrons in the molybdenum sulfide conduction band reduce the silver ions to the nano silver particles, and the holes in the iron oxide oxidize the water to oxygen. In addition, it was reported that carbon doping could create empty 2p orbitals perpendicular to the basal plane, enabling energetically favorable water adsorption and dissociation, which indicates the formation of Fe–C and Mo–C bond could be beneficial to the catalytic reaction.[42]

4. Conclusion

In this work, (MoS_2, γ-Fe_2O_3)/graphene catalyst of well-constructed MoS_2/graphene/Fe_2O_3 heterojunctions was synthesized *via* one-step calcination of MoS_2@Fe-MOF composite. The

 This journal is © The Royal Society of Chemistry 2020

Open Access Article. Published on 01 May 2020. Downloaded on 2/13/2026 8:04:32 PM.
This article is licensed under a Creative Commons Attribution-NonCommercial 3.0 Unported Licence.

(MoS_2, γ-Fe_2O_3)/graphene catalyst produce 4400 μmol g^{-1} h^{-1} of oxygen under visible light irradiation, which is more than twice compared to that of γ-Fe_2O_3/graphene. The Z scheme band-alignment between MoS_2 and γ-Fe_2O_3 and the high conductivity of graphene as a transfer channel of photo-generated electrons result in enhanced efficiency of charge separation and remarkable performance of catalyst in water oxidation reaction. This work provides a novel method to design a highly efficient catalyst *via* constructing effective hetero-junctions for photocatalytic water oxidation and other photo-catalysis reactions.

Conflicts of interest

There are no conflicts to declare.

References

1 D. Gust, T. A. Moore and A. L. Moore, *Acc. Chem. Res.*, 2009, **42**, 1890–1898.
2 A. J. Bard and M. A. Fox, *Acc. Chem. Res.*, 1995, **28**, 141–145.
3 H. Tong, S. Ouyang, Y. Bi, N. Umezawa, M. Oshikiri and J. Ye, *Adv. Mater.*, 2012, **24**, 229–251.
4 X. B. Chen, S. H. Shen, L. J. Guo and S. S. Mao, *Chem. Rev.*, 2010, **110**, 6503–6570.
5 S. R. Pendlebury, M. Barroso, A. J. Cowan, K. Sivula, J. Tang, M. Graetzel, D. Klug and J. R. Durrant, *Chem. Commun.*, 2011, **47**, 716–718.
6 J. Tang, J. R. Durrant and D. R. Klug, *J. Am. Chem. Soc.*, 2008, **130**, 13885–13891.
7 M. Mishra and D.-M. Chun, *Appl. Catal., A*, 2015, **498**, 126–141.
8 G. Wang, Y. Ling, D. A. Wheeler, K. E. N. George, K. Horsley, C. Heske, J. Z. Zhang and Y. Li, *Nano Lett.*, 2011, **11**, 3503–3509.
9 C. J. Sartoretti, M. Ulmann, B. D. Alexander, J. Augustynski and A. Weidenkaff, *Chem. Phys. Lett.*, 2003, **376**, 194–200.
10 L. Li, Y. Yu, F. Meng, Y. Tan, R. J. Hamers and S. Jin, *Nano Lett.*, 2012, **12**, 724–731.
11 F. B. Li, X. Z. Li, C. S. Liu and T. X. Liu, *J. Hazard. Mater.*, 2007, **149**, 199–207.
12 Z. Zhang, M. F. Hossain, T. Miyazaki and T. Takahashi, *Environ. Sci. Technol.*, 2010, **44**, 4741–4746.
13 M. Rioult, H. Magnan, D. Stanescu and A. Barbier, *J. Phys. Chem. C*, 2014, **118**, 3007–3014.
14 G. K. Pradhan, N. Sahu and K. M. Parida, *RSC Adv.*, 2013, **3**, 7912–7920.
15 G. K. Pradhan, S. Martha and K. M. Parida, *ACS Appl. Mater. Interfaces*, 2012, **4**, 707–713.
16 D. Bi and Y. Xu, *J. Mol. Catal. A: Chem.*, 2013, **367**, 103–107.
17 J. Zhu, Z. Yin, D. Yang, T. Sun, H. Yu, H. E. Hoster, H. H. Hng, H. Zhang and Q. Yan, *Energy Environ. Sci.*, 2013, **6**, 987–993.
18 L. Li, Y. Chu, Y. Liu and L. Dong, *J. Phys. Chem. C*, 2007, **111**, 2123–2127.
19 T. K. Townsend, E. M. Sabio, N. D. Browning and F. E. Osterloh, *Energy Environ. Sci.*, 2011, **4**, 4270–4275.
20 Y. Q. Cong, Y. H. Ge, T. T. Zhang, Q. Wang, M. L. Shao and Y. Zhang, *Ind. Eng. Chem. Res.*, 2018, **57**, 881–890.
21 Q. Xiang, J. Yu and M. Jaroniec, *J. Phys. Chem. C*, 2011, **115**, 7355–7363.
22 Q. Li, B. Guo, J. Yu, J. Ran, B. Zhang, H. Yan and J. R. Gong, *J. Am. Chem. Soc.*, 2011, **133**, 10878–10884.
23 Y. H. Ng, A. Iwase, A. Kudo and R. Amal, *J. Phys. Chem. Lett.*, 2010, **1**, 2607–2612.
24 S. C. Han, L. F. Hu, Z. Q. Liang, S. Wageh, A. A. Al-Ghamdi, Y. S. Chen and X. S. Fang, *Adv. Funct. Mater.*, 2014, **24**, 5719–5727.
25 L. X. Chen, F. He, N. Q. Zhao and R. S. Guo, *Appl. Surf. Sci.*, 2017, **420**, 669–680.
26 K. Shen, X. D. Chen, J. Y. Chen and Y. W. Li, *ACS Catal.*, 2016, **6**, 5887–5903.
27 J. Yao, J. Y. Chen, K. Shen and Y. W. Li, *J. Mater. Chem. A*, 2018, **6**, 3571–3582.
28 Q. Li, P. Xu, W. Gao, S. G. Ma, G. Q. Zhang, R. G. Cao, J. Cho, H.-L. Wang and G. Wu, *Adv. Mater.*, 2014, **26**, 1378–1386.
29 F. Xie, G.-P. Lu, R. Xie, Q.-H. Chen, H.-F. Jiang and M. Zhang, *ACS Catal.*, 2019, **9**, 2718–2724.
30 W. Chaikittisilp, K. Ariga and Y. Yamauchi, *J. Mater. Chem. A*, 2013, **1**, 14–19.
31 J. Xie, H. Zhang, S. Li, R. Wang, X. Sun, M. Zhou, J. Zhou, X. W. Lou and Y. Xie, *Adv. Mater.*, 2013, **25**, 5807–5813.
32 Y. Horiuchi, T. Toyao, K. Miyahara, L. Zakary, V. Dang Do, Y. Kamata, T.-H. Kim, S. W. Lee and M. Matsuoka, *Chem. Commun.*, 2016, **52**, 5190–5193.
33 J. Shao, Z. Wan, H. Liu, H. Zheng, T. Gao, M. Shen, Q. Qu and H. Zheng, *J. Mater. Chem. A*, 2014, **2**, 12194–12200.
34 W. Wu, X. H. Xiao, S. F. Zhang, T. C. Peng, J. Zhou, F. Ren and C. Z. Jiang, *Nanoscale Res. Lett.*, 2010, **5**, 1474–1479.
35 R. Li, L. Yang, T. Xiong, Y. Wu, L. Cao, D. Yuan and W. Zhou, *J. Power Sources*, 2017, **356**, 133–139.
36 Y.-Y. Li, J.-H. Wang, Z.-J. Luo, K. Chen, Z.-Q. Cheng, L. Ma, S.-J. Ding, L. Zhou and Q.-Q. Wang, *Sci. Rep.*, 2017, **7**, 7178.
37 L. Zhang, X. Wang, R. Wang and M. Hong, *Chem. Mater.*, 2015, **27**, 7610–7618.
38 M. Lotya, Y. Hernandez, P. J. King, R. J. Smith, V. Nicolosi, L. S. Karlsson, F. M. Blighe, S. De, Z. Wang, I. T. McGovern, G. S. Duesberg and J. N. Coleman, *J. Am. Chem. Soc.*, 2009, **131**, 3611–3620.
39 H. A. Becerril, J. Mao, Z. Liu, R. M. Stoltenberg, Z. Bao and Y. Chen, *ACS Nano*, 2008, **2**, 463–470.
40 W. Kou, G. Chen, Y. Liu, W. Guan, X. Li, N. Zhang and G. He, *J. Mater. Chem. A*, 2019, **7**, 20614–20623.
41 X. Xue, J. Zhang, I. A. Saana, J. Sun, Q. Xu and S. Mu, *Nanoscale*, 2018, **10**, 16531–16538.
42 Y. Zang, S. Niu, Y. Wu, X. Zheng, J. Cai, J. Yee, Y. Xie, Y. Liu, J. Zhou, J. Zhu, X. Liu, G. Wang and Y. Qian, *Nat. Commun.*, 2019, **10**, 1217.
43 J. Wan, X. Du, E. Liu, Y. Hu, J. Fan and X. Hu, *J. Catal.*, 2017, **345**, 281–294.
44 J. Liu, Y. Liu, N. Liu, Y. Han, X. Zhang, H. Huang, Y. Lifshitz, S.-T. Lee, J. Zhong and Z. Kang, *Science*, 2015, **347**, 970–974.

Open Access Article. Published on 01 May 2020. Downloaded on 2/13/2026 8:04:32 PM.
This article is licensed under a Creative Commons Attribution-NonCommercial 3.0 Unported Licence.

45 W. Chen, Y. Zhou, L. Wang, Y. Wu, B. Tu, B. Yu, F. Liu, H.-W. Tam, G. Wang, A. B. Djurisic, L. Huang and Z. He, *Adv. Mater.*, 2018, **30**, 1800515.
46 Y. Karpov, T. Erdmann, I. Raguzin, M. Al-Hussein, M. Binner, U. Lappan, M. Stamm, K. L. Gerasimov, T. Beryozkina, V. Bakulev, D. V. Anokhin, D. A. Ivanov, F. Gunther, S. Gemming, G. Seifert, B. Voit, R. Di Pietro and A. Kiriy, *Adv. Mater.*, 2016, **28**, 6003–6010.
47 J. Wang, P. Guo, M. Dou, J. Wang, Y. Cheng, P. G. Jonsson and Z. Zhao, *RSC Adv.*, 2014, **4**, 51008–51015.
48 Z.-F. Huang, L. Pan, J.-J. Zou, X. Zhang and L. Wang, *Nanoscale*, 2014, **6**, 14044–14063.
49 Z. Jiang, W. Wan, H. Li, S. Yuan, H. Zhao and P. K. Wong, *Adv. Mater.*, 2018, **30**, 1706108.
50 L. J. Zhang, S. Li, B. K. Liu, D. J. Wang and T. F. Xie, *ACS Catal.*, 2014, **4**, 3724–3729.

 This journal is © The Royal Society of Chemistry 2020